Computational Analysis of Three-Dimensional Turbulent Flow Around a Bluff Body in Ground Proximity

Taeyoung Han*
General Motors Research Laboratories, Warren, Michigan

The Reynolds-averaged Navier-Stokes equations, together with the equations of the k-ϵ model of turbulence, were solved numerically in a general curvilinear coordinate system for three-dimensional turbulent flows around Ahmed's vehicle-like body. The numerical computations were performed for various afterbody upper-surface slant angles at a constant Reynolds number of 4.3×10^6 based on the body length. A multistep correction procedure was incorporated into the incompressibility condition, and the solution of the Poisson equation for pressure was obtained from the conjugate gradient method. A second-order discretization scheme for the convection term was applied to reduce the numerical diffusion. Most of the essential measured features of the flowfield around Ahmed's vehicle-like body in ground proximity, such as the formation of trailing vortices and the reverse flow region resulting from separation, were well predicted.

Introduction

THE study of three-dimensional flow over a ground vehicle has become a subject of significant importance in the automobile industry. One obvious way of improving the fuel economy of vehicles is to reduce aerodynamic drag by optimizing the body shape. Execution of a good aerodynamic design under stylistic constraints requires extensive understanding of the flow phenomena and, especially, of how the aerodynamic forces are influenced by changes in body shape. The aerodynamic forces are caused by various viscous flow phenomena, such as the three-dimensional turbulent boundary layer on the body surface, longitudinal vortices induced by three-dimensional separation, recirculating flows caused by separation, and the ground-plane boundary layer. The interactions among these phenomena are even more complex.

Although computation has proved to be very useful in many areas of fluid mechanics, the complexity of flows around bluff bodies has discouraged practical computational work in this area. Obviously, experiments will play a significant role in providing qualitative and quantitative understanding of the flow around bluff bodies; however, numerical methods for interpreting and guiding the experiments are also important. One of the main aims of vehicle aerodynamics is to predict the influence of changes in body shape on the flow and hence on the drag. The availability of a reliable numerical prediction method could greatly reduce the design costs by minimizing the amount of wind-tunnel testing required.

The accuracy and efficiency of the theoretical predictions for various viscous flow phenomena depends directly on the choice of the mathematical model and on the numerical solution procedure. A number of numerical methods[1-4] have been developed for compressible flows. These methods are based on either finite-volume or finite-difference techniques, solve for fluid density directly from the continuity equation, and obtain the pressure from the equation of state. However, these methods may not be applied directly to predict flows around automobiles where the flow is essentially incompressible. Implementing these methods for simulating incompressible flow is not efficient. Since there is no variation in density, the round-off error from the computer can easily destroy the accuracy of the predicted pressure field.

Presented as Paper 88-3766 at the 1st National Fluid Dynamics Congress, Cincinnati, OH, July 25-28, 1988; received Aug. 22, 1988; revision received Dec. 13, 1988.

*Staff Research Engineer, Engineering Mechanics Dept.

Several other numerical methods[5-7] have been proposed for solving the incompressible, three-dimensional, Navier-Stokes equations in curvilinear coordinates. These methods are based on either the pressure-correction method[8] or the artificial compressibility method.[9] In the present study, the former is used due to its simplicity as well as its economy of computation time. A more efficient pressure-correction method, pressure implicit split operator (PISO),[10] is extended to nonorthogonal curvilinear coordinates and is incorporated into the incompressibility condition. The solution of the Poisson equation for pressure is obtained with the conjugate gradient (CG) method,[11] while the solution of the transport equations are obtained with the tridiagonal matrix algorithm (TDMA).[12] A central differencing scheme is used to discretize the convection and diffusion terms in the governing equations.

The present study is a preliminary investigation based on a relatively simple bluff body and aimed at future applications to realistic automobile shapes. The selected body should generate the essential features of a real vehicle flowfield. This study focuses on the separated wake structure that contains both longitudinal and transverse vortices and on the prediction of the aerodynamic drag due to the afterbody slant angle.

The selection of the experiment to be computationally modeled will be discussed first. In a following section, the governing equations and turbulence closure modeling are considered. The numerical procedure and mesh generation method are then discussed, followed by a comparison of numerical results with the experimental data.

Ahmed's Body

Through a literature survey, Ahmed's vehicle-like body[13] (which is a variant of the original Morel's body[14]) was selected to be computed because of well-defined body geometry and available experimental data at a high Reynolds number of 4.3×10^6 (based on the body length). No computational work has been reported for this experiment. This is one of the few experiments conducted with a bluff body in ground proximity where surface pressure and time-averaged wake data are available. A similar body was studied by Morel,[14] but only limited data were reported. Ahmed's body has an overall length of 1.044 m and length:width:height ratios of 3.36 : 1.37 : 1. The body surface grid is shown in Fig. 1. The body consists of a forebody, a midsection, and a rear end. The forebody is rounded to achieve a separation-free flow over its surface. Interchangeable rear ends allowed investigation of the effect of slant angle on drag. All rear ends had same slant length of 0.222 m and had sharp edges. The flow

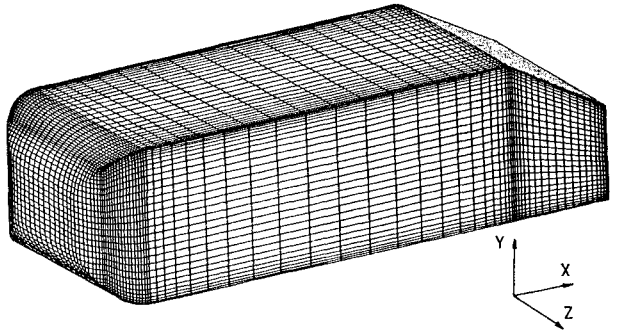

Fig. 1 Surface grid distribution (97 × 51 × 31) on Ahmed's body with 30-deg slant angle.

studied here had a freestream velocity of 60 m/s, which corresponds to a Reynolds number of 4.3×10^6. The flow around this body is influenced strongly by the angle of the rear slant surface, which indicates that the large portion of aerodynamic drag is generated by the development of three-dimensional vortex separation from the rear slant surface.

Governing Equations

The governing equations are derived from the Reynolds-averaged Navier-Stokes equations with an eddy viscosity approximation. These governing equations can be expressed in Cartesian tensor form as

Continuity:

$$\frac{\partial u_i}{\partial x_i} = 0 \tag{1}$$

Momentum:

$$\frac{\partial}{\partial x_i}(u_i u_j) = -\frac{1}{\rho}\frac{\partial p}{\partial x_j} + \frac{\partial}{\partial x_i}\left[(\nu + \nu_t)\left(\frac{\partial u_i}{\partial x_j} + \frac{\partial u_j}{\partial x_i}\right) - \frac{2}{3}\delta_{ij}k\right] \tag{2}$$

where u_i, p, and ρ are the mean velocity, mean pressure, and density, respectively. In order to get closure of the above system of equations, the eddy viscosity ν_t is related to the turbulent kinetic energy k and its rate of dissipation ϵ by

$$\nu_t = C_\mu \frac{k^2}{\epsilon} \tag{3}$$

where C_μ is a constant, and k and ϵ are obtained from standard k-ϵ turbulence model[15] equations.

In order to treat general curved boundaries, the independent space variables (x,y,z) in the governing equations are transformed to a body-fitted coordinate system (ξ,η,ζ), leaving the velocity components (u,v,w) in the Cartesian (x,y,z) coordinates. Using the standard transformation formulae, the continuity equation becomes

$$U_\xi + V_\eta + W_\zeta = 0 \tag{4}$$

and the five transport equations for $\phi = u,v,w,k$, and ϵ can be expressed in the compact form as follows:

$$\begin{aligned}(U\phi)_\xi + (V\phi)_\eta + (W\phi)_\zeta = &\left[\frac{\Gamma^\phi}{J}(D_{11}^2 + D_{12}^2 + D_{13}^2)\phi_\xi\right]_\xi \\ &+ \left[\frac{\Gamma^\phi}{J}(D_{21}^2 + D_{22}^2 + D_{23}^2)\phi_\eta\right]_\eta \\ &+ \left[\frac{\Gamma^\phi}{J}(D_{31}^2 + D_{32}^2 + D_{33}^2)\phi_\zeta\right]_\zeta + S^\phi J\end{aligned} \tag{5}$$

where subscripts ξ, η, and ζ denote derivatives along those coordinates.

The detailed expressions of the source term S^ϕ can be found in Han.[16] The contravariant variables U, V, and W,

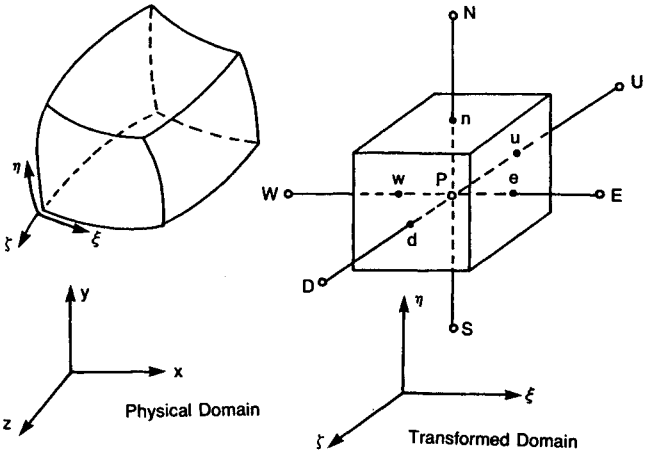

Fig. 2 Curvilinear coordinates and finite-volume representation.

which represent convective flux at the boundaries, are given by

$$U = D_{11}u + D_{12}v + D_{13}w \tag{6a}$$

$$V = D_{21}u + D_{22}v + D_{23}w \tag{6b}$$

$$W = D_{31}u + D_{32}v + D_{33}w \tag{6c}$$

The geometric coefficients D_{ij} and the Jacobian J, which appear in the above equations are functions of the coordinates only and are defined as:

$$D_{ij} = \begin{vmatrix} y_\eta z_\zeta - y_\zeta z_\eta & x_\zeta z_\eta - x_\eta z_\zeta & x_\eta y_\zeta - x_\zeta y_\eta \\ y_\zeta z_\xi - y_\xi z_\zeta & x_\xi z_\zeta - x_\zeta z_\xi & x_\zeta y_\xi - x_\xi y_\zeta \\ y_\xi z_\eta - y_\eta z_\xi & x_\eta z_\xi - x_\xi z_\eta & x_\xi y_\eta - x_\eta y_\xi \end{vmatrix} \tag{7a}$$

$$J = x_\xi y_\eta z_\zeta + x_\zeta y_\xi z_\eta + x_\eta y_\zeta z_\xi - x_\xi y_\zeta z_\eta - x_\eta y_\xi z_\zeta - x_\zeta y_\eta z_\xi \tag{7b}$$

These geometric coefficients are obtained directly from central differencing in the transformed plane.

Method of Computation

Discretization

Discretized finite-difference forms of the governing differential equations are obtained using a finite-volume approach. All the dependent and independent variables are stored at the same grid location and variables at the finite control-volume boundaries are interpolated between adjacent grid points by a simple averaging. However, the central differencing of the convection terms causes instability in the solution due to a lack of diagonal dominance in the resulting matrix when the cell Reynolds number ($= U \cdot \Delta X/\nu$) exceeds two. Diagonal dominance of the matrix with central differencing can be obtained from various techniques.[5,17] In the present study, the following upwind inertia flux scheme is used in order to enhance the diagonal dominance. The variable at the finite-volume boundaries are specified depending on the sign of the flux U_e:

If $U_e \geq 0$,

$$\phi_e = (\phi_E + \phi_P)/2 + K(\phi_P - \phi_E) - K(\phi_P^o - \phi_E^o) \tag{8a}$$

If $U_e < 0$,

$$\phi_e = (\phi_E + \phi_P)/2 + K(\phi_E - \phi_P) - K(\phi_E^o - \phi_P^o) \tag{8b}$$

where the subscript e denotes the finite-volume boundary location between grid points P and E (see Fig. 2). The

superscript o denotes "old" values from previous iteration level. The constant K can be chosen to make the diagonal term dominant. When we specify the value 0.5 for K, the present numerical scheme produces a fully upwind operator in an implicit form, but the final converged solution will satisfy second-order accuracy with favorable numerical stability. However, a major problem associated with the central differencing of convection terms for high Reynolds number flows is the appearance of spatial oscillations in the solution. In order to suppress these "wiggles" in the solution, some form of artificial viscosity must be included in the numerical scheme. In the present study, an implicit form of the second-order dissipation term[18] is used. With these representations, a finite-difference analog of the general transport equation, Eq. (5), then can be expressed as

$$A_P\phi_P = A_E\phi_E + A_W\phi_W + A_N\phi_N + A_S\phi_S + A_D\phi_D + A_U\phi_U + S^\phi J \tag{9}$$

where the subscripts P,N,S,E,W,U, and D denote locations of nodal points as shown in Fig. 2. The coefficients A_E, A_W, etc., involve contributions due to the convective fluxes as well as diffusive fluxes in the ξ, η, and ζ directions.

Pressure-Velocity Correction Method

In the present study, a two-step correction procedure known as pressure implicit split operator (PISO)[10] has been used in both the pressure and the velocity corrections for nonorthogonal curvilinear coordinates. The two-step correction procedure is described as follows.

Predictor Stage

The three intermediate velocity components are obtained by solving the three momentum equations with the pressure field, p^n, at the nth iteration:

$$u_j^* = \frac{\sum A_m\, u_{jm}^* - D_{ij}\Delta_i p^n + S_j^n}{A_P} \tag{10}$$

where A is the coefficient shown in Eq. (9), m the grid node identifier, and the summation is over the six surrounding grid nodes. The mass fluxes across the boundaries of the cells are obtained from the velocity field:

$$U_i^* = \frac{D_{ij}}{A_P}\left(\sum A_m u_{jm}^* - D_{ij}\Delta_i p^n + S_j^n\right) \tag{11}$$

where the geometric coefficient D_{ij} is defined in Eq. (7). These mass fluxes do not in general satisfy mass conservation; corrections on the pressure and velocity are made based on the two corrector steps.

Corrector Stage

New mass fluxes U_i^{**} are established to enforce the local mass conservation with a corresponding new pressure field p^*.

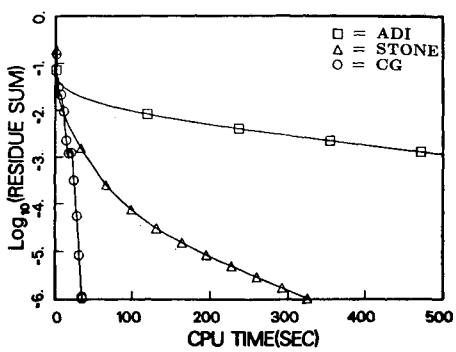

Fig. 3 Comparison of convergence history of three different pressure solvers with the CPU time for a (97 × 51 × 31) mesh.

This corrector stage is split into the two corrector steps.

First step:

$$U_i^{**} = \frac{D_{ij}}{A_P}\left(\sum A_m u_{jm}^* - D_{ij}\Delta_i p^* + S_j^n\right) \tag{12}$$

Second step:

$$U_i^{***} = \frac{D_{ij}}{A_P}\left(\sum A_m u_{jm}^{**} - D_{ij}\Delta_i p^{**} + S_j^n\right) \tag{13}$$

where $(\,)^*$ denotes the newly updated values. Here, the corrections are split into two steps where operations on pressure are separated from those on velocity. By subtracting Eq. (11) from Eq. (12) and subtracting Eq. (12) from Eq. (13), respectively, and imposing the divergence-free conditions $\Delta_i U_i^{**}$ and $\Delta_i U_i^{***} = 0$, the following pressure correction equations are obtained:

First correction:

$$\Delta_i\left[\frac{D_{ij}^2}{A_P}\Delta_i\,(p^* - p^n)\right] = \Delta_i U_i^* + \lambda \tag{14}$$

where λ is the dissipation term to be explained in the next section.

Second correction:

$$\Delta_i\left[\frac{D_{ij}^2}{A_P}\Delta_i(p^{**} - p^*)\right] = \Delta_i\left[\frac{D_{ij}}{A_P}\sum A_m(u_{jm}^{**} - u_{jm}^*)\right] \tag{15}$$

The first correction is identical to the semi-implicit method for pressure linked equations (SIMPLE)[8] algorithm which includes only the effect of pressure gradient. The second correction is a complementary step for the effect of convection and diffusion terms.

In the present work, the system of algebraic equations formed by pressure-correction equations, Eqs. (14) and (15), produce a seven-banded matrix that is symmetric and positive definite. The solution of this matrix is the most time-consuming part in the present numerical computation. It is crucial to incorporate a very efficient and practical algorithm in solving these equations for a large size. The conjugate gradient (CG)[11] method is regarded as an excellent one for the solution of a symmetric, positive-definite matrix. The ultimate success of the CG method depends on the quality of the preconditioning. Preconditioning is often required to produce a transformed matrix with more favorable properties, such as eigenvalue clustering that accelerates convergence. In the present work, a simple diagonal scaling[19] is used as the preconditioner. The performance (measured by CPU time) of the CG method with diagonal scaling is shown in Fig. 3. The popular alternating direction implicit (ADI)[12] method and Stone's strongly implicit method (STONE)[20] are directly compared with the CG method. As shown in Fig. 3, the CG method is far superior to the two other methods. The CPU time per iteration for the CG method is roughly 8 times less than Stone's method and about 10 times less than the ADI method on the CRAY-XMP/24. The real advantages of the CG method are that the algorithm does not depend on arbitrary parameters, that the exact solution can be obtained in a finite number of steps, and that the algorithm is highly vectorizable.

Higher-Order Smoothing Terms

It is well known that the nonstaggered grid arrangement generates an alternating spatial instability in the pressure field due to the decoupling effect between velocities and pressures. In the present work, the nonstaggered grid arrangement is used with an explicit fourth-order pressure dissipation term that was developed by Rhie and Chow[21] in solving two-dimensional viscous flow problems. The term λ in the right-

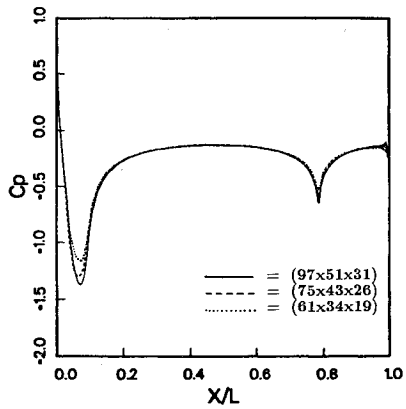

Fig. 4 Effect of grid refinement on the top surface symmetry plane static pressure distribution for 12.5-deg slant angle.

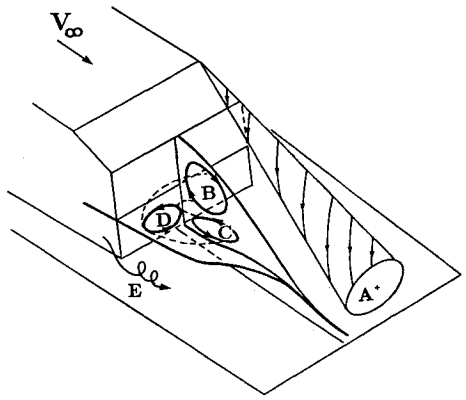

Fig. 5 Schematic of three-dimensional wake pattern behind Ahmed's body with slanted rear surface.

handside of Eq. (14) is as follows:

$$\lambda = \frac{C}{4}[A_e^p(p_{EE} - 3p_E + 3p_P - p_W) - A_w^p(p_E - 3p_P + 3p_W - p_{WW}) + A_n^p(p_{NN} - 3p_N + 3p_P - p_S) - A_s^p(p_N - 3p_P + 3p_S - p_{SS}) + A_d^p(p_{DD} - 3p_D + 3p_P - p_U) - A_u^p(p_D - 3p_P + 3p_U - p_{UU})] \quad (16)$$

where A_e^p, A_w^p, etc., are the coefficients of the pressure correction equation from Eq. (14). It was found in the present study that the converged solution is insensitive to the value of C when $0.1 < C < 0.5$.

Initial and Boundary Conditions

In the present work, a potential flowfield is specified throughout the computational domain as an initial condition for the three-dimensional viscous flow calculations. A three-dimensional panel code[22] employing flat panels with constant source strengths was implemented for initializing the present code. It takes roughly 2 min of CPU time for the initialization of the velocity field around a body with approximately 600 body surface panels.

Ahmed's body was tested in open jet wind tunnels[13] with a ground plane 3 m wide and 5 m long. About 1.35 body length of ground plane projected in front and 2.45 body length behind the model. No velocity distributions are reported in the inlet and the outer boundaries. In the present study, the potential flow solution is employed to specify three-component velocities at the inlet and at the outer boundaries. The inlet plane is located at the leading edge of the ground plane and zero boundary-layer thickness is assumed. The turbulent kinetic energy and its dissipation rate are specified at the inlet assuming local equilibrium of turbulence. The exit plane is located at roughly 5 body lengths downstream of the body and the constant-pressure boundary condition is imposed. Symmetry boundary conditions are enforced at the symmetry plane. At the body surface and the ground plane, no-slip boundary conditions are imposed. Near the wall, the standard log-law wall functions[15] are used for the velocity distribution.

Computational Grid

A simple sheared grid system was generated by applying algebraic stretching with a hyperbolic tangent function. In order to check the numerical sensitivity of the solution to the grid refinement, computed surface pressures with three different mesh refinements ($61 \times 34 \times 19$, $75 \times 43 \times 26$, and $97 \times 51 \times 31$) were compared. As shown in Fig. 4, the results of the $97 \times 51 \times 31$ mesh is probably accurate enough to be regarded as a grid-independent solution. Therefore, all the computations presented here are based on the same number of mesh points ($97 \times 51 \times 31$). Later, the grids were refined up to a $121 \times 71 \times 47$ mesh in order to check the influence of further grid refinement on the drag coefficient; a negligible change in the drag coefficient was found.

It is estimated that the CPU time per point and iteration (on the CRAY-XMP/24), including data input/output, is about 2×10^{-4} S. It takes about 200 iterations to reduce the total mass residue by three orders of magnitude for a $75 \times 43 \times 26$ mesh. The drag coefficient was converged roughly after 200 iterations. Therefore, it takes roughly 1 h of CPU time for one complete calculation for a $75 \times 43 \times 26$ mesh.

Computational Results

The method described in the previous section has been tested for a variety of two-dimensional flows. Here, we present some three-dimensional computational results for Ahmed's vehicle-like body.[13] Ahmed's experimental study includes a drag breakdown, a detailed survey of the body surface static pressure distribution, and the time-averaged wake structure for various rear slant angles.

Comparison of Predicted and Experimental Flowfields

The main features of the flow around the afterbody are illustrated in Fig. 5. This schematic of the flow phenomena is based on the present computations and the results of Ahmed's experimental study. The three-dimensional boundary layer from the slanted side edge rolls up into a pair of trailing vortices A. At the top and bottom edges of the flat vertical base, the shear layer develops into two recirculating flow regions B and C. Although it is not mentioned in Ahmed's experimental study, the present work indicates the presence of another pair of recirculating flow regions D, which is generated from the left and right edges of the flat vertical base, as shown in Fig. 5. The size and shape of these recirculating vortices are strongly influenced by the slant angle, as will be discussed. Counter-rotating vortices E (shown in Fig. 5) near the ground plane occur due to the viscous interaction between the body and the ground-plane boundary layers.

The computed flow will be summarized by presenting results in the plane of symmetry, a horizontal plane, and a few transverse planes in the downstream wake. Figure 6 shows the change of the wake structure in the plane of symmetry for slant angles of 0, 5, 12.5, and 25 deg. The relative sizes of vortices B and C are strongly dependent on the slant angle due to the formation of trailing vortices A and the change of vertical base area. As the flow over the slant surface is strongly influenced by the trailing vortices coming off the side edges, the shape and the size of the upper recirculating flow B is dependent upon the amount of the downwash from the outer field into the recirculating region. At 25 deg, the upper recirculating flow B is strongly dominant compared to the lower recirculating flow C. Figure 7 shows the change of the

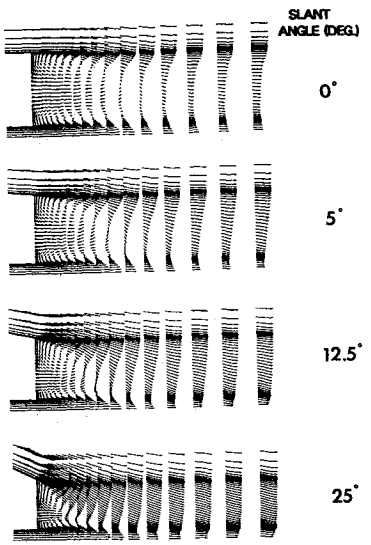

Fig. 6 Wake pattern in the plane of symmetry for slant angles of 0, 5, 12.5, and 25 deg.

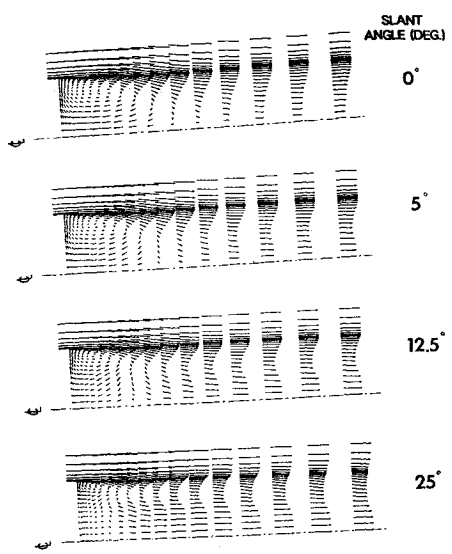

Fig. 7 Wake pattern in the horizontal plane for slant angles of 0, 5, 12.5, and 25 deg.

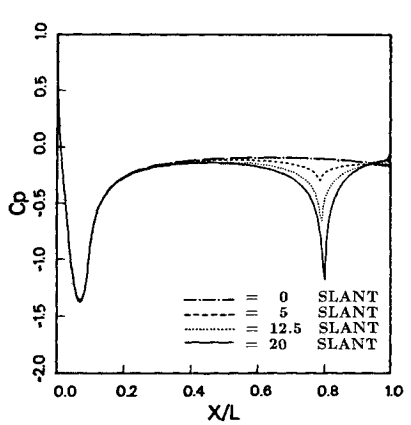

Fig. 8 Top surface symmetry plane static pressure distribution for slant angles of 0, 5, 12.5, and 20 deg.

flow pattern in a horizontal plane located at the middle of the vertical base for a given slant angle. As the separation bubble length decreases with increasing slant angle, the size and the strength of vortex D decreases. As shown in Fig. 7, the

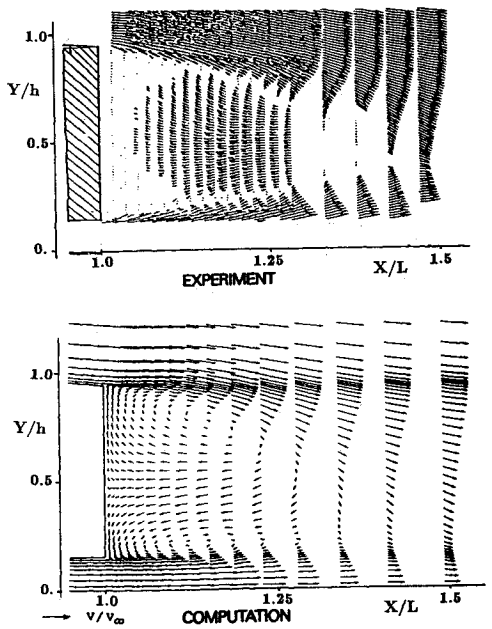

Fig. 9 Comparison of the experimental and computational wake velocity vector distribution in the symmetry plane behind Ahmed's body with a 5-deg slant angle.

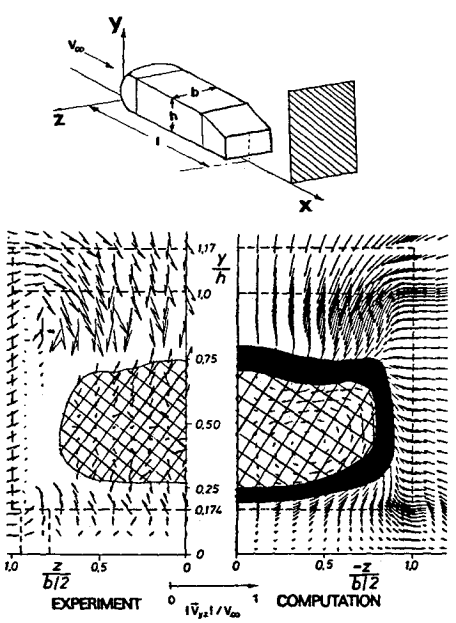

Fig. 10 Comparison of cross-flow velocity distributions in the transverse plane at $X/L = 1.115$ (12.5-deg slant angle).

velocity profile downstream of the separation bubble changes considerably with the slant angle. The local minimum of the velocity profile, which was located along the symmetry plane for the zero slant angle, moves away from the symmetry plane as the slant angle increases. The trailing vortices A coming off the side edges generate the downwash into the symmetry plane. This downwash induces relatively high momentum flow along the symmetry plane downstream of the separation bubble.

The computed pressure distribution along the top surface in the plane of symmetry for slant angles of 0, 5, 12.5, and 20 deg is shown in Fig. 8. Since there were no noticeable differences in the surface pressures on the forebody with considerable shape changes in the afterbody, the interaction between the rear and the front is very weak. This is a consequence of the relatively long midsection and was also indicated by Ahmed et al.[13]

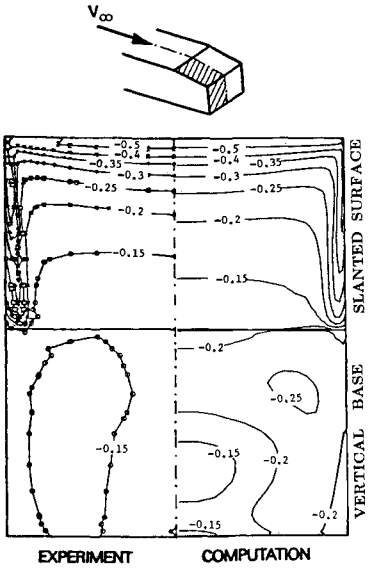

Fig. 11 Comparison of static pressure contours on the rear-end surface (12.5-deg slant angle).

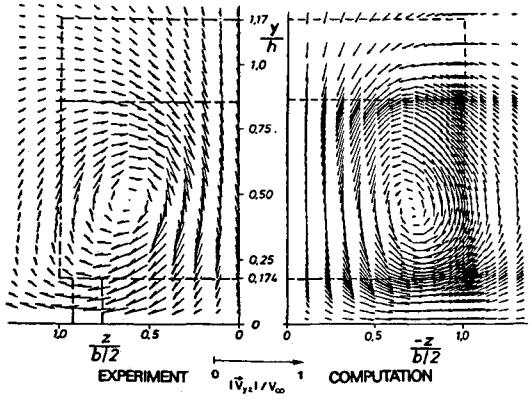

Fig. 12 Comparison of crossflow velocity distribution in the transverse plane at $X/L = 1.479$ (25-deg slant angle).

Comparison of the experimental and computational velocity vector distribution in the plane of symmetry of the wake is shown in Fig. 9 for the slant angle of 5 deg. The two recirculating flows B and C are clearly visible both in the experiment and the computations. The experiments and the computed results are very similar.

The velocity vector field in a transverse plane near the model base is shown in Fig. 10 for the 12.5 deg slant angle. The computed results are again qualitatively very similar to the experimental data. The region of reverse flow is represented by the cross-hatched area both for the computation and experiment. It is difficult to draw the boundary of the reverse flow region from the experimental measurements because of the small magnitude of the velocity head near the boundary of the reverse flow region. Ahmed's 10 hole directional probe[13] has errors of up to 1% of freestream dynamic pressure, which corresponds to 10% errors in the velocity measurement. Therefore, the boundary of the reverse flow region for the computation is defined within the accuracy limit of the experimental data. The overall shape of the reversed flow region is very similar for the computation and the experiment.

Figure 11 shows the static pressure isobars on the unfolded rear end surface for a 12.5 deg slant angle. Fairly good agreement between the experiment and computation can be seen over the entire slanted surface, except near the vertical base. Relatively low base pressure was predicted on the rear vertical base, and this decreased the surface pressure near the

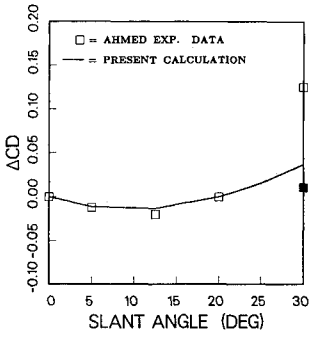

Fig. 13 Incremental change of total drag coefficient with slant angle (dark symbol represents the experimental data above the critical slant angle).

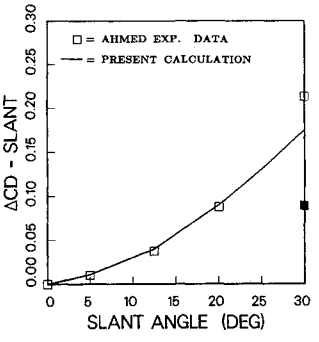

Fig. 14 Drag change at the slant surface with slant angle.

downstream end of the slanted surface compared with the experimental data.

Figure 12 shows the velocity distribution for a slant angle of 25 deg in the downstream transverse plane at $X/L = 1.479$ where the separation bubble closes and the overall flow is dominated by the trailing vortex A. The location and the size of the vortex are very well predicted.

Comparison of Predicted and Experimental Forces

Here, we will present a quantitative comparison between the computed and experimental aerodynamic forces for Ahmed's body. It is well known that contribution of skin-friction drag to the total drag is less significant for bluff bodies. In Ahmed's experiment, the skin-friction drag coefficients varied between 0.047 to 0.055, which corresponded to roughly 20% of the total drag. Therefore, about 80% of the total drag is due to the pressure drag. The computed skin-friction drag was found to vary between 0.047 and 0.049.

The computed total drag coefficient including the skin-friction drag is 0.33 at a slant angle of 0 deg, which is considerably higher than the experimental value of 0.25. The difference between computation and experiment in the drag coefficient is due mainly to a relatively low predicted value of the base pressure and partly to numerical inaccuracy associated with the sheared grid structure on the forebody. Figure 13 shows the incremental change of the drag coefficient, using the zero slant case as a reference, with the slant angle. As shown in Fig. 13, the drag coefficient initially decreased with increasing slant angle, reaching a minimum near 12 deg corresponding to approximately a 0.02 drop in drag coefficient from the value at 0 deg slant angle. This initial decrease in drag is due to pressure recovery on the slanted surfaces, which also increases the base pressure. The strength of the trailing vortices increases strongly beyond 12 deg, and the drag coefficient increases rapidly. The computed results predict the overall trend and are quantitatively accurate up to a slant angle of 20 deg. Beyond 20 deg, the experimental drag coefficient increases very rapidly, while the computed values increase much less rapidly. The difference between the computation and the experiment in drag coefficient near 30 deg is

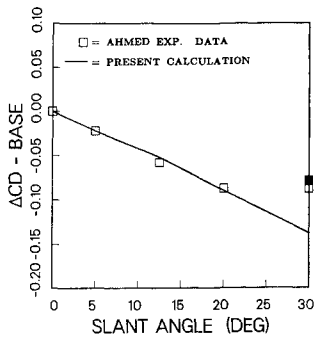

Fig. 15 Drag change at the vertical base with slant angle.

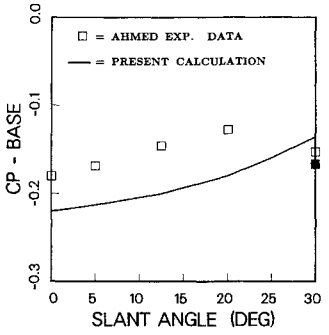

Fig. 16 Variation of average base pressure coefficient with slant angle.

due to underprediction of the pressure drag both from the vertical base and the slanted surface, since the drag contributed by the forebody and skin-friction drag are nearly constant for all slant angles. The contributions to the pressure drag from the slanted surface and from the vertical base are shown in Figs. 14 and 15. The changes of drag on the slanted surface and the vertical base are very well predicted up to 20 deg. However, the underprediction of the drag near the 30 deg is due to an insufficient strength of the trailing vortex in the prediction and the underprediction of the base pressure. As shown in Fig. 16, the average base pressure coefficient increases with the slant angle up to 20 deg for both computation and experiment. However, the experimental data show a decrease of the base pressure near the critical angle, while the predicted value continuously increases.

The maximum drag coefficient occurred at the slant angle of 30 deg, and this was immediately followed by a sharp drop in drag coefficient due to the breakdown of the trailing vortices at higher angles (shown as dark symbols in Figs. 13 and 14). It was observed[14] that the flow is highly unstable at this critical angle and the flow pattern changes abruptly with a small disturbance. The computations were not pursued beyond the 30-deg slant angle, since the phenomena of the vortex breakdown over the slanted surface was not properly captured in the predictions.

Conclusions

The present study illustrated the capabilities of the present method and also indicated areas that require further study. The overall accuracy of these numerical predictions depends both on the validity of the turbulence model and the accuracy of the numerical schemes applied to solve the Navier-Stokes equations. The present analysis predicted most of the essential features of the flowfield around Ahmed's body in ground proximity, such as the formation of trailing vortices and the reverse flow region from separation. However, the accurate prediction of drag coefficient for three-dimensional bluff bodies requires further development of turbulence modeling. In the present study, the k-ϵ turbulence model consistently underpredicted the base pressure. While the numerical accuracy is considered to be a significant error source in the overall prediction, the turbulence modeling becomes equally important for the correct prediction of the base pressure and the strength of the trailing vortices.

Acknowledgments

The author would like to acknowledge helpful discussions with D. C. Hammond and C. A. Koromilas. Thanks are also due to Prof. V. C. Patel for reviewing the paper and for helpful discussions.

References

[1]Martinelli, L., Jameson, A., and Grasso, F., "A Multigrid Method for the Navier-Stokes Equations," AIAA Paper 86-0208, Jan. 1986.

[2]Briley, W. R. and McDonald, H., "Solutions of the Multi-Dimensional Compressible Navier-Stokes Equations by a Generalized Implicit Method," *Journal of Computational Physics*, Vol. 24, Aug. 1977, pp. 372–397.

[3]MacCormack, R. W., "A Numerical Method for Solving the Equations of Compressible Viscous Flow," *AIAA Journal*, Vol. 20, 1982, pp. 1275–1281.

[4]Beam, R. M. and Warming, R. F., "An Implicit Factored Scheme for the Compressible Navier-Stokes Equations," *AIAA Journal*, Vol. 16, April 1978, pp. 393–402.

[5]Rhie, C. M., "A Pressure Based Navier-Stokes Solver Using the Multigrid Mehtod," AIAA Paper 86-0207, Jan. 1986.

[6]Hah, C., "A Navier-Stokes Analysis of Three-Dimensional Turbulent Flows Inside Turbine Blade Rows at Design and Off-Design Conditions," *Transactions of ASME, Journal of Engineering for Power*, Vol. 106, April 1984, pp. 421–429.

[7]Kwak, D., "An Incompressible Navier-Stokes Flow Solver in Three-Dimensional Curvilinear Coordinate System Using Primitive Variables," AIAA Paper 84-0253, Jan. 1984.

[8]Patankar, S. V. and Spalding, D. B., "A Calculation Procedure for Heat, Mass and Momentum Transfer in Three-Dimensional Parabolic Flows," *International Journal of Heat and Mass Transfer*, Vol. 15, Oct. 1972, pp. 1787–1806.

[9]Chorin, A. J., "Numerical Solution of the Navier-Stokes Equations," *Mathematics of Computation*, Vol. 22, No. 104, 1968, pp. 745–762.

[10]Issa, R. I., "Solution of the Implicitly Discretized Fluid Flow Equations by Operator-Splitting," *Journal of Computational Physics*, Vol. 62, Jan. 1986, pp. 40–65.

[11]Hestenes, M. R. and Stiefel, E., "Methods of Conjugate Gradients for Solving Linear Systems," *Journal of Research of the National Bureau of Standards*, Vol. 49, March 1952, pp. 409–436.

[12]Peaceman, D. W. and Rachford, H. F., "The Numerical Solution of Parabolic and Elliptic Differential Equations," *Journal Society Industrial Applied Mathematics*, Vol. 3, March 1955, pp. 28–41.

[13]Ahmed, S. R., Ramm, G., and Faltin, G., "Some Salient Features of the Time-Averaged Ground Vehicle Wake," Society of Automotive Engineers, Warrendale, PA, SAE Paper 840300, Feb. 1984.

[14]Morel, T., "Aerodynamic Drag of Bluff Body Shapes Characteristic of Hatch-Back Cars," Society of Automotive Engineers, Warrendale, PA, SAE Paper 780267, Feb. 1978.

[15]Launder, B. E. and Spalding, D. B., "The Numerical Calculation of Turbulent Flows," *Computational Methods in Applied Mechanics and Engineering*, Vol. 3, March 1974, pp. 269–289.

[16]Han, T., "A Navier-Stokes Analysis of Three-Dimensional Turbulent Flows around a Bluff Body in Ground Proximity," AIAA Paper 88-3766, July 1988.

[17]Han, T., Humphrey, J. A. C., and Launder, B. E., "A Comparison of Hybrid and Quadratic-Upstream Differencing in High Reynolds Number Elliptic Flows," *Computational Methods in Applied Mechanics and Engineering*, Vol. 29, March 1981, pp. 81–95.

[18]Liu, N. S., Shamroth, S. J., and McDonald, H., "Numerical Solution of the Navier-Stokes Equations for Compressible Turbulent Two/Three Dimensional Flows in the Terminal Shock Region of an Inlet/Diffuser," AIAA Paper 83-1892, July 1983.

[19]El Tahry, S. H., private communication, Dec. 1985.

[20]Stone, H. L., "Iterative Solution of Implicit Approximation of Multi-dimensional Partial Differential Equations," *SIAM Journal of Numerical Analysis*, Vol. 5, Sept. 1968, pp. 530–558.

[21]Rhie, C. M. and Chow, W. L., "Numerical Study of the Turbulent Flow Past an Airfoil with Trailing Edge Separation," *AIAA Journal*, Vol. 21, Nov. 1983, pp. 1525–1532.

[22]Koromilas, C. A., private communication, June 1985.